ACS Photonics

Article

Cite This: ACS Photonics 2019, 6, 99−106

pubs.acs.org/journal/apchd5

Photonic Spin Hall Effect in Robust Phase Gradient Metasurfaces Utilizing Transition Metal Nitrides

Krishnakali Chaudhuri,[†] Amr Shaltout,[†,‡] Deesha Shah,[†] Urcan Guler,[†] Aveek Dutta,[†] Vladimir M. Shalaev,[†] and Alexandra Boltasseva*[,†]

[†]School of Electrical & Computer Engineering and Birck Nanotechnology Center, Purdue University, West Lafayette, Indiana 47907, United States

[‡]Geballe Lab for Advanced Materials, Stanford University, Stanford, California 94305, United States

Supporting Information

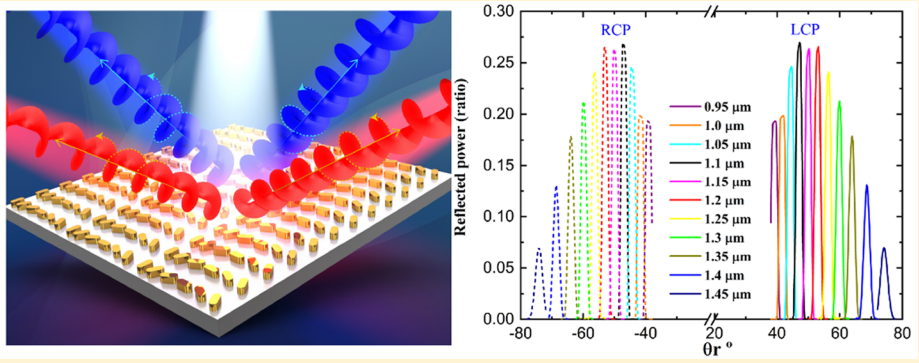

ABSTRACT: Robust and high-temperature stable (refractory) transition metal nitrides are an emerging class of nanophotonic materials aimed at durable, bio- and CMOS-compatible plasmonic and metasurface applications. In this work, we experimentally demonstrate titanium nitride- and zirconium nitride-based phase manipulating optical metasurfaces that exhibit a photonic spin Hall effect. In the developed all-nitride system, metal nitrides are combined with dielectric nitrides such as aluminum nitride and silicon nitride to design a highly anisotropic, multilayer resonator geometry that supports gap plasmons and enables high power efficiency (∼40%) and broad bandwidth of operation in the near-infrared wavelength region. A one-dimensional phase gradient created by geometric rotations of the resonators leads to simultaneous, spatial separation of right and left circular polarization as well as different frequency components of the incident light. This work shows that transition metal nitrides can be successfully integrated into efficient metasurface building blocks for planar, rugged optical devices.

KEYWORDS: *metasurface, refractory plasmonics, titanium nitride, zirconium nitride, photonic spin Hall effect*

Metasurfaces embody a vast range of planar optical devices that achieve advanced control of light propagation, amplitude, and phase by employing carefully designed metallic and/or dielectric optical scatterers at the interface.[1,2] In the past decade, numerous demonstrations have employed planar metasurface architecture to realize a wide variety of optical elements,[3] ultracompact flat lenses,[4−6] planar holograms,[7−9] wave-plates,[10−13] spectrometers,[14−17] and polarization rotators.[18−21] Among them, plasmonic metasurfaces provide a unique capability enabled by metallic resonators, as they confine electromagnetic energy beyond the diffraction limit and enhance light−matter interactions, leading to significant scale-down of the device footprint.[22] Plasmonic metasurfaces have been proven beneficial when it comes to augmenting bio-, molecular, or chemical sensing,[23−25] detection,[26] energy harvesting,[27−29] and even information encoding systems.[30−32] However, all metallic components suffer from finite optical losses that may negatively impact the device efficiency in many cases.[33,34] On the other hand, low-loss dielectric materials may improve the metasurface device efficiency but often at the cost of relatively intensive fabrication, high-aspect-ratio requirement, and more bulky resonator structures.[35,36] Recently, a multilayered, metal−insulator−metal stacked resonator geometry has emerged as a complementary approach that combines high efficiency and compactness.[37,38] A periodic array of metal nanoantennas placed on a metal back plane, separated by a thin dielectric layer, supports gap surface plasmon (GSP) resonances and enables improved amplitude and phase control in metasurfaces.[39,40]

Along with the optimally efficient geometry, selection of constituent materials is yet another crucial part of metasurface design. In the case of plasmonics, the two most prolifically used metallic components for optical metasurfaces are gold (Au) and silver (Ag). These noble metals show excellent plasmonic

Received: July 11, 2018
Published: November 13, 2018

DOI: 10.1021/acsphotonics.8b00943
ACS Photonics 2019, 6, 99−106

behavior in the visible to near-infrared (NIR) spectral range as well as strong chemical inertness (for Au).[41] Most plasmonic metasurfaces have therefore been built utilizing these metals. However, with the expanding reach of metasurface functionalities, limitations of the existing materials become apparent. When considered for practical devices, noble metals pose significant challenges.[42−44] Owing to their relatively low melting point when nanostructured and high malleability, noble metals' applicability is limited in practical devices requiring high temperature stability, robustness to high-intensity lasers, mechanical durability, stable growth into ultrathin films, and CMOS process compatibility for on-chip applications. In contrast, transition metal nitrides (TMNs) have been gaining attention as a robust and CMOS-compatible plasmonic platform for harsh environment applications.[45−47]

Metallic TMNs such as titanium nitride (TiN), zirconium nitride (ZrN), hafnium nitride (HfN), niobium nitride (NbN), and tantalum nitride (TaN) have been used in a variety of electronic applications since the early 1980s.[48,49] Generally, these conductive ceramics display high mechanical durability and, more importantly, a strong refractory nature, that is, very high bulk melting points (>3000 °C). TiN and ZrN are commonly used as hard, protective coatings for medical equipment and mechanical parts. In appearance they closely resemble Au and are often used as its cheaper alternatives in large-scale manufacturing as well. In addition, most of the constituent transition metals (Ti, Ta, Hf) as well as some nitrides (TiN, TaN) are already-existing parts of the CMOS process.[50,51] Their mechanical properties, similar optical properties to noble metals, and CMOS compatibility have led the interest of the plasmonics research community to metal nitrides. Following the first reports of the useful plasmonic properties of titanium nitride and, zirconium nitride,[42,49,52,53] their growth techniques and material and optical properties have been rigorously investigated.[54−58] The plasma frequencies of both TiN and ZrN are in the visible range, but they typically exhibit larger optical losses as compared to commonly used noble metals. Strong optical nonlinearity,[59−61] temperature-dependent complex dielectric permittivity,[62,63] and elevated damage threshold of the nitrides[61,64,65] allow for stable device operation in various harsh environment conditions. In addition, the binary nature of the nitrides provides room to tailor the optical properties via varying the stoichiometry. The optical response of the TMNs depends on many factors including the lattice structure, crystal defects, surface roughness, grain sizes, stoichiometry, and so on. As a result of differing growth parameters during thin film deposition in the literature, the optical properties of the metal nitrides vary within a large spectrum.[48] High-quality thin films are typically obtained on specific substrate materials and at elevated deposition temperatures that present additional constraints to the achievable device design and pose challenges in their integration into planar optical devices.[54,66,67]

The growing knowledge base of plasmonic metal nitrides has naturally led to the development of practical metamaterial and metasurface designs in the past years. Broadband perfect absorbers,[65,68] local heat sources,[69] and arbitrary lattice optics[70] using TiN planar structures are particularly noteworthy applications that have utilized the lossy nature of nitrides as well as their plasmonic property. Here, for the first time, we introduce the plasmonic metal nitrides to the realm of plasmonic phase-gradient metasurfaces employing GSP resonances in multilayered, metallic nanoantennas (NAs) to create a desired spatial phase profile and manipulate the propagating wavefront. We have experimentally illustrated a photonic spin Hall effect (SHE) in the NIR, by reflecting the two-spin states (right circular and left circular polarizations, RCP and LCP) in the opposite directions with mirror-symmetric angular dispersion of the frequency components, as shown in the schematic of Figure 1, realizing a circular dichroism

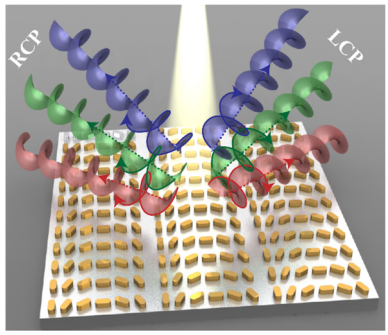

Figure 1. Schematic of the metasurface exhibiting a photonic spin Hall effect (SHE) by separating the two circular polarizations (or photonic spins) in opposite angular directions.

spectrometer. Circular dichroism (CD) spectrometers are used extensively in biological sensing and pharmaceutical application spaces to detect the chirality of molecules that have different optical responses to circularly polarized light components.[71,72] Typically, a CD spectrometer operates by sequentially switching between the LCP and RCP at the input.[73] A metasurface-based approach achieves this complex operation by simultaneously generating the two polarization (spin) states with high efficiency in a planar, ultrathin, lightweight device and can therefore eliminate the need for typical bulky and expensive spectrometers and polarization switchable sources. An optical metasurface device with this functionality was previously introduced by Shaltout et. al. using subwavelength Au nanoantenna elements.[16] Based on a similar approach, a geometric phase gradient metasurface displaying photonic SHE is designed and implemented for both TiN- and ZrN-based nanoantenna elements. The nitride-based metasurface spectrometer can further reduce the cost, increase durability of the device, and be integrated in *in situ* biocompatible sensing tools as well. This work emphasizes the ability to integrate the refractory plasmonic metal nitrides into practically realizable, planar optical devices.

We measured the spectral profile of the complex dielectric function (ε) of thin films of TiN and ZrN and compared them to well-known noble metals, Au and Ag. TiN and ZrN are deposited using DC reactive magnetron sputtering, whereas the Au and Ag films are deposited using electron beam evaporation. A variable-angle spectroscopic ellipsometry (VASE) setup (Figure S1) is used to measure the optical response of the films, which is then fitted to an analytical model (containing Drude- and Lorentz-type oscillators) to extract the complex permittivity, ε (eq S1, Table S1). A dielectric to metallic crossover for the real part of the permittivity ε' at ∼500 nm (for TiN) and ∼400 nm (for ZrN) indicates plasmonic behavior in part of the visible range and NIR. In the spectral range of 0.5−2 μm, both TiN and ZrN behave as metals (large negative real part of permittivity, ε', Figure 2(a)) similar to Au and Ag. but at the same time exhibit a relatively higher magnitude of the imaginary part of

DOI: 10.1021/acsphotonics.8b00943
ACS Photonics 2019, 6, 99−106

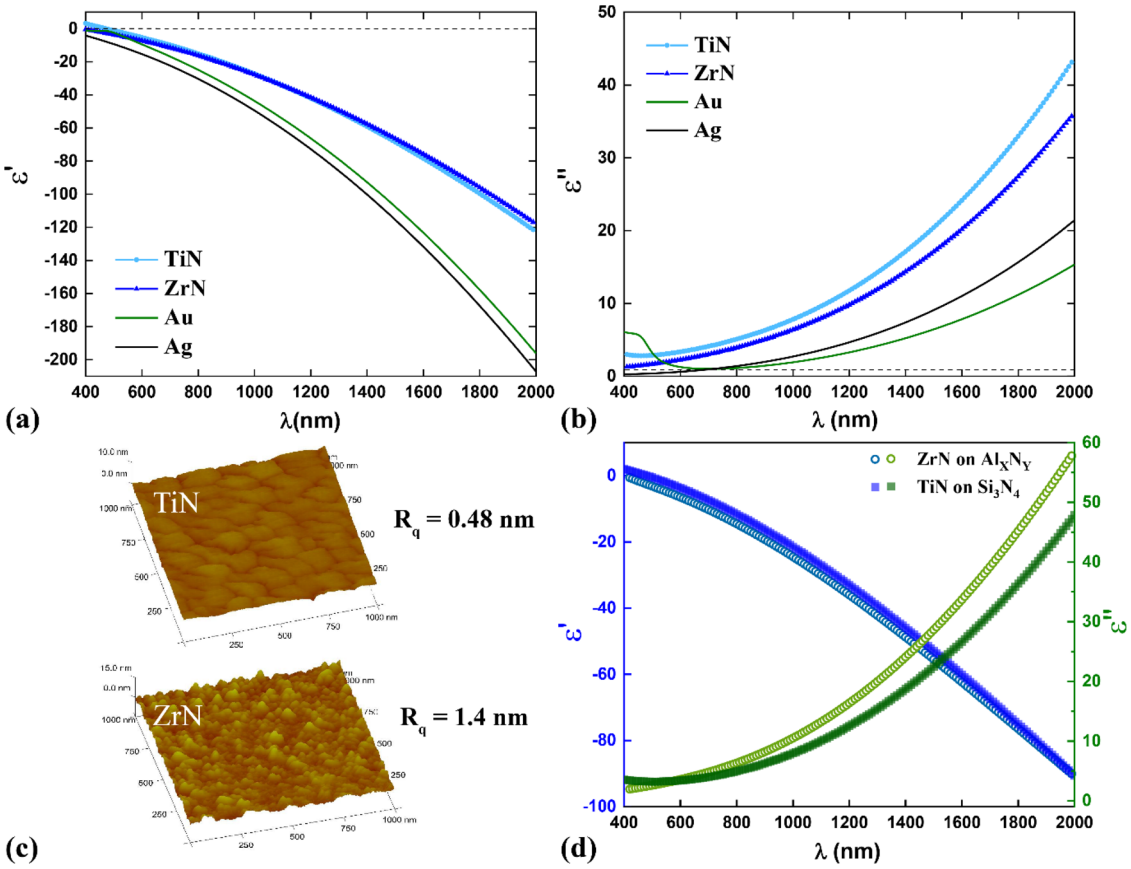

Figure 2. Comparison of experimentally measured real (ε') (a) and imaginary (ε'') (b) parts of the complex dielectric function (ε) of TiN, ZrN, Au, and Ag films of thickness ~200 nm (optically thick). TiN and ZrN films are deposited on a crystalline MgO substrate and Au and Ag films are deposited on fused silica/glass substrate. (c) Surface roughness of corresponding TiN and ZrN films measured using atomic force microscopy (AFM) technique. Measured root mean square (rms) values of surface roughness (R_q) are indicated. (d) Experimentally measured real (ε') (left axis, blue) and imaginary (ε'') (right axis, green) parts of complex ε of polycrystalline TiN (~70 nm) and ZrN (~80 nm) grown on amorphous dielectrics Al_xN_y and Si_3N_4, respectively.

the permittivity, ε'', indicating larger optical losses in these films (Figure 2(b)). The losses stem from the interband electronic transitions, represented by the Lorentz oscillators (eq S1, Table S1) as well as electron−electron, electron−phonon, surface defects, and grain boundary scattering processes experienced by the large number of free electrons in the lattice. Surface roughness of the films are measured using an atomic force microscopy (AFM) technique. The AFM scanned images collected from the nitride films are presented in Figure 2(c). The plasmonic behavior of transition metal nitrides is critically dependent on their fine crystal structure, which is largely affected by the growth conditions as well as the nature of the underlying substrate. The epitaxial growth of TiN on a lattice-matched, single-crystalline MgO substrate results in a much lower surface roughness and larger grain boundaries for TiN (0.48 nm (rms)) as compared to polycrystalline ZrN (1.4 nm (rms)) on MgO. In the case of the multilayered, GSP-type resonator structure used in the metasurface design, the optical properties of the top metal layer grown on a thin dielectric are also critical. Therefore, we look at the experimentally measured complex permittivity dispersions of the TiN grown on silicon nitride (Si_3N_4) and the ZrN grown on aluminum nitride (Al_xN_y) (Figure 2(d)). Nitride-based dielectrics are chosen over more commonly used oxides (such as Al_2O_3 or SiO_2) to avoid oxygen contamination into the metal nitride. Silicon nitride and aluminum nitride are high-refractive-index dielectrics that confine the gap-plasmon resonating mode and are deposited using chemical vapor deposition (CVD) and DC sputtering, respectively. The amorphous nature of the dielectrics leads to polycrystalline structures of the top TiN and ZrN layers, resulting in reduced metallicity and increased optical losses (see Figure 2(d)). Measured ε' are compared for Al_xN_y and Si_3N_4 in Figure S2. These measured optical properties of all constituent layers of the resonator are input into the multiphysics simulation (for details, see Supporting Information, section 1) to achieve an optimized geometry.

A photonic SHE is generated from the interaction of photon spin or the polarization state of light and asymmetric nanostructured antennas.[17,74,75] Unique arrangements of the anisotropic resonating elements create different phase gradients seen by the two circular polarized (RCP and LCP) components of the incident light. To achieve high efficiency of operation, a reflection mode unit cell supporting gap-plasmon-type resonance was chosen. The unit cell consists of a rectangular brick-shaped plasmonic NA made of TiN or ZrN placed on a bilayer metal−dielectric stack (Figure 3(a−c)). This geometrical configuration supports a GSP resonance mode which achieves strong confinement of the electromagnetic energy to the narrow dielectric (spacer/gap) region.[76] The forward and backward propagating surface plasmons (SPs) at the two adjacent dielectric−metal interfaces interfere constructively and destructively to create standing

DOI: 10.1021/acsphotonics.8b00943
ACS Photonics 2019, 6, 99−106

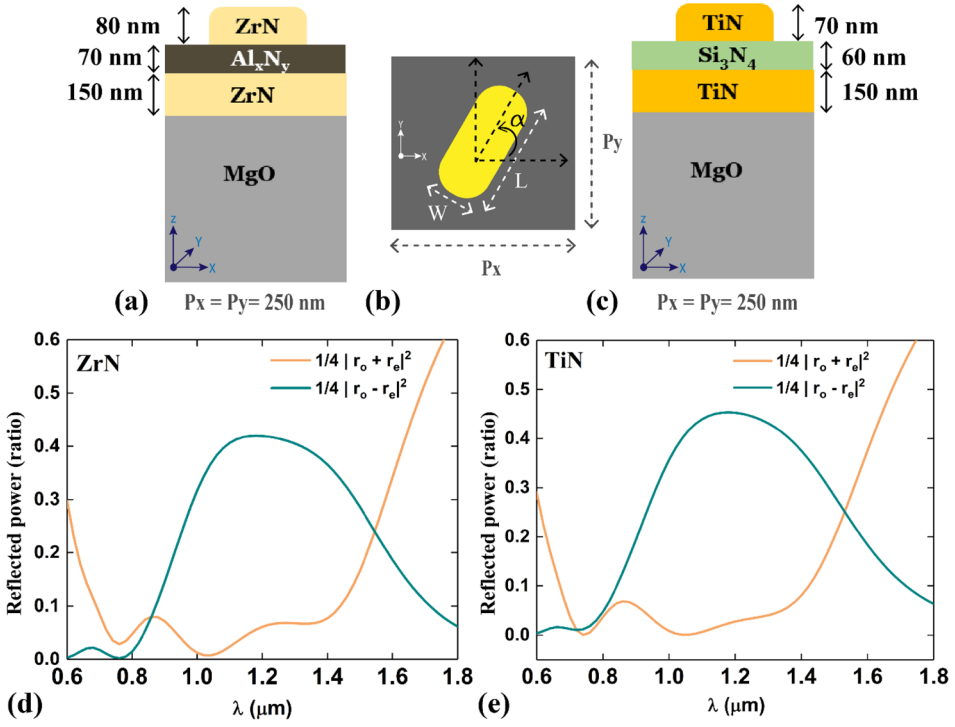

Figure 3. (a) Cross-section view of ZrN−Al_xN_y−ZrN-based unit cell (optimized thickness for each layer is indicated). (b) Top-view schematic of a single NA element rotated at an angle of α. Edges are rounded to make the design realistic for fabricated structures. (c) Cross-section of TiN−Si_3N_4−TiN-based unit cell (optimized thickness for each layer is indicated). Simulation results for both ZrN (d) and TiN (e) based meta-unit array showing maximum power output to the copolarized component (indicated by $1/4|(r_o - r_e)|^2$) while the power reflected to the normal cross-polarized mode (indicated by $1/4|(r_o + r_e)|^2$) is minimized.

wave resonances in a Fabry−Perot-like cavity at certain frequencies, which causes the high electric field confinement in the gap region. This enhances the quality factor of the resonance, which in turn improves the power efficiency of the metasurface device as compared to devices with a single layer of metal NA unit cells. Strong coupling of the incident light into the GSP resonance mode also allows for large phase accumulation.[37,39] With the optimum aspect ratio (length/width) of the rectangular NA, a π-phase delay between the reflection coefficient components along the major and minor axes can be achieved.

To arrive at an optimal geometry, first a single unit cell (meta-unit) response is theoretically analyzed. The polarization and phase state of the reflected light beam is represented by Jones calculus. The Jones matrix for an anisotropic NA element can be written as[77]

$$\hat{M} = \hat{R}(-\alpha)\begin{pmatrix} r_o & 0 \\ 0 & r_e \end{pmatrix}\hat{R}(\alpha) \tag{1}$$

where r_o and r_e are reflection coefficients for incident light polarized along the two principal axes of the antenna. $\hat{R}(\alpha)$ denotes the rotation matrix, and α is the rotation angle of the resonating element (indicated in Figure 3(b)),

$$\hat{R}(\alpha) = \begin{pmatrix} \cos\alpha & \sin\alpha \\ -\sin\alpha & \cos\alpha \end{pmatrix} \tag{2}$$

Equation 1 can be rewrittern in circular basis as[77,78]

$$\hat{M}_{\text{circular}} = \begin{pmatrix} \frac{1}{2}(r_o - r_e)e^{-i2\alpha} & \frac{1}{2}(r_o + r_e) \\ \frac{1}{2}(r_o + r_e) & \frac{1}{2}(r_o - r_e)e^{i2\alpha} \end{pmatrix} \tag{3}$$

For a right- or left-handed circular polarized incident light ($E_i^{R/L}$), the reflected light from the anisotropic meta unit, $E_r^{R/L}$ is expressed as

$$E_r^{R/L} = \hat{M}.\, E_i^{R/L} \tag{4}$$

$$E_r^{R/L} = \frac{1}{2}(r_o + r_e)E_i^{L/R} + \frac{1}{2}(r_o - r_e)e^{im2\alpha}E_i^{R/L} \tag{5}$$

The first term on the right-hand side (RHS) of eq 5 represents the circularly polarized reflected light component that has the opposite spin state to the incident one, and the second term on the RHS is the part with the same photon spin state. This second component is the copolarized component of reflected light associated with an additional geometric Panchratnam−Berry phase[79] of magnitude $m2\alpha$, where $m = \begin{cases} -1, \text{ for RCP} \\ +1, \text{ for LCP} \end{cases}$ incident light. This phase gradient term can attain any value within the entire 2π phase space by geometric rotation of the meta-units. The first term on the RHS represents the cross-polarized reflected light component that has no phase dependence.

All geometric dimensions of the meta-units are varied to obtain maximum power reflected into the copolarized mode while simultaneously minimizing the efficiency of the cross-polarized mode. This is attained at frequencies where r_o and r_e are out of phase with each other. Design optimization was

DOI: 10.1021/acsphotonics.8b00943
ACS Photonics 2019, 6, 99−106

performed through full-wave 3D finite element method (FEM) simulation using the commercially available Multiphysics solver COMSOL. The optimized dimensions of each meta-unit are indicated in Figure 3(a,c). In one device, the 80 nm thick ZrN NA sits on a stack of 70 nm thick aluminum nitride (Al_xN_y) spacer on a 150 nm thick ZrN (mirror) film. In the other one, the bilayer stack consists of a 60 nm thick silicon nitride (Si_3N_4) spacer on 150 nm thick TiN mirror, and the top TiN NA is 70 nm thick. The top rectangular brick NA is 95 nm wide (W) and 205 nm long (L) in both cases. Figure 3(d,e) plot the simulated power efficiency to both co- and cross-polarized components that are $1/4|(r_o - r_e)|^2$ and $1/4|(r_o - r_e)|^2$, respectively, for the two designs. A high (>40%) reflection efficiency is achieved in both cases, which is comparable to the previously demonstrated Au-based counterpart.[16] The larger optical losses of the TMNs are tackled through optimization of the nanoantenna design to arrive at this comparable efficiency and a much broader bandwidth (the full width at half-maximum (fwhm) of the copolarized component) of operation. The ZrN- and TiN-based designs should, therefore, exhibit a photonic SHE in the spectral window of ~0.9−1.6 μm (Figure 3(d,e)).

With this optimized structure, a supercell was created from a linear arrangement of six meta-units. In the supercell, each meta-unit is rotated at an angle of |30°| relative to the neighboring one, as shown in the schematic in Figure 4(a,b). This provides a uniform phase gradient along the x-axis. The two circular polarized components of incident wave of this one-dimensional phase gradient are opposite in sign, causing them to reflect in opposite directions. A periodic array of the supercell over a large area makes the final metasurface device. The device performance is estimated by simulating the periodic supercell array. The spatial electric field maps shown in Figure 4(c,d) show that the incident LCP and RCP components are anomalously reflected in two opposite angular directions. This angle of reflection measured in simulation is further verified by the well-known generalized Snell's law[80] as $\theta = \sin^{-1}\left(m\frac{\lambda}{P}\right)$, where P is the supercell periodicity (1.5 μm in this case), λ is the reflected wavelength, and m is as before. Each frequency component is reflected at a different anomalous angle, creating a spatially dispersed spectra of the copolarized light. The supercell period was chosen to be 1.5 μm to keep the angular dispersion of the operating bandwidth (0.9−1.6 μm) at an angle greater than 38°, a limitation posed by the experimental measurement setup (see Supporting Information, Section 2).

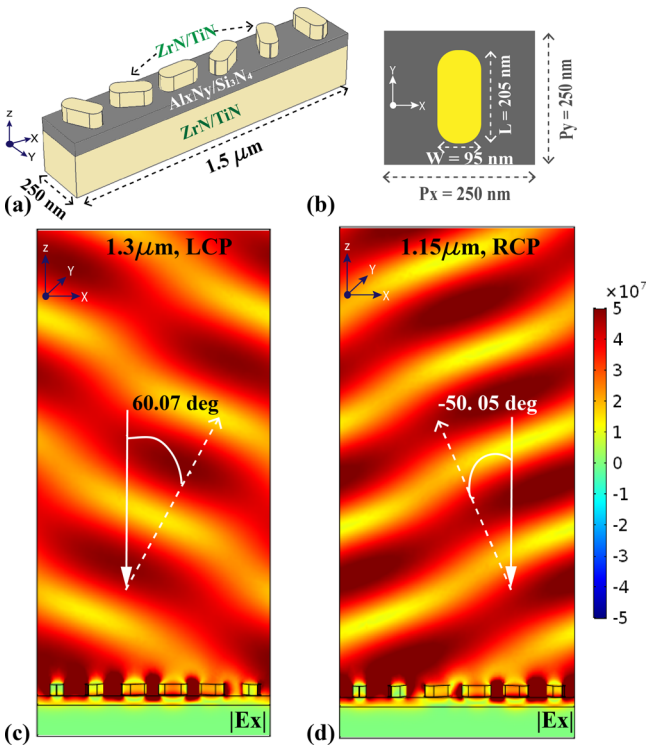

Figure 4. Schematic of (a) the complete supercell and (b) a single brick-shaped NA as in the simulation. (c, d) Electric field (|Exl) map of the simulated response of a TiN−Si_3N_4−TiN-based design showing an electromagnetic wave anomalously reflected in opposite directions, at an angle of $\theta \approx 60°$ for 1.3 μm LCP (c) and at $\theta \approx -50°$ for 1.15 μm RCP (d) incident wave (colorbar indicates amplitude).

To fabricate the designed metasurfaces, first, the metal−dielectric−metal stack was created on a crystalline MgO substrate using a bottom-up growth technique. This was followed by top-down electron beam lithography and dry halogen plasma etching to define the metallic NA elements (for details, see the Supporting Information, Section 1). The top-down, cross-section, and tilted view of the scanning electron microscope (SEM) images of a fabricated metasurface are shown in Figure 5(a−c).

A VASE (Figure S1) setup is used to experimentally measure the response of the fabricated metasurface. The setup employs a tunable monochromatic source and a polarizer, followed by a retarder device to generate circularly polarized waves. A rotating detector arm allows for collecting the anomalously reflected light as a function of angular dispersion. Experimentally measured angular dispersions from the two fabricated metasurface devices are plotted in Figure 5(d,e). Photonic SHE is illustrated as the opposite spin components (LCP and RCP) of incident light are reflected in the mirror symmetric directions. Each color on the plots (Figure 5(d,e)) represents a different frequency component, and the peak positions are as obtained by the generalized Snell's law. As in spectrometers, this creates a spatial dispersion of the frequency spectrum. Our experimental setup restricts the collection of light reflected at angles of <38° (that corresponds to λ < 0.94 μm for a supercell period of 1.5 μm). The reflected power efficiency reaches a maximum of ~28% at 1.1 μm for the TiN-based device (~19% at 1.04 μm for the ZrN-based one) and gradually decreases for both lower and higher frequencies as expected from the simulation results shown in Figure 3(d,e).

Patterning films into nanoscale antenna geometry is known to increase effective optical losses of plasmonic metals owing to large scattering from the edges and surface roughness resulting from chemically reactive high energy plasma etching processes. These factors adversely affect the device performance and reduce power efficiency of the fabricated metasurface.[81] Betterment of the optical properties of the unpatterned continuous films of TiN and ZrN and replacement of the chemically reactive high energy etching process step with a lift-off-type technique is expected to improve power efficiency further (see Supporting Information, Section 3, Figure S3).

In this work, we designed, fabricated, and characterized two phase gradient metasurfaces utilizing refractory plasmonic metal nitrides, TiN and ZrN, that exhibit a photonic spin Hall effect by separating in reflection the two opposite spin components of the incident light. The measured power

DOI: 10.1021/acsphotonics.8b00943
ACS Photonics 2019, 6, 99−106

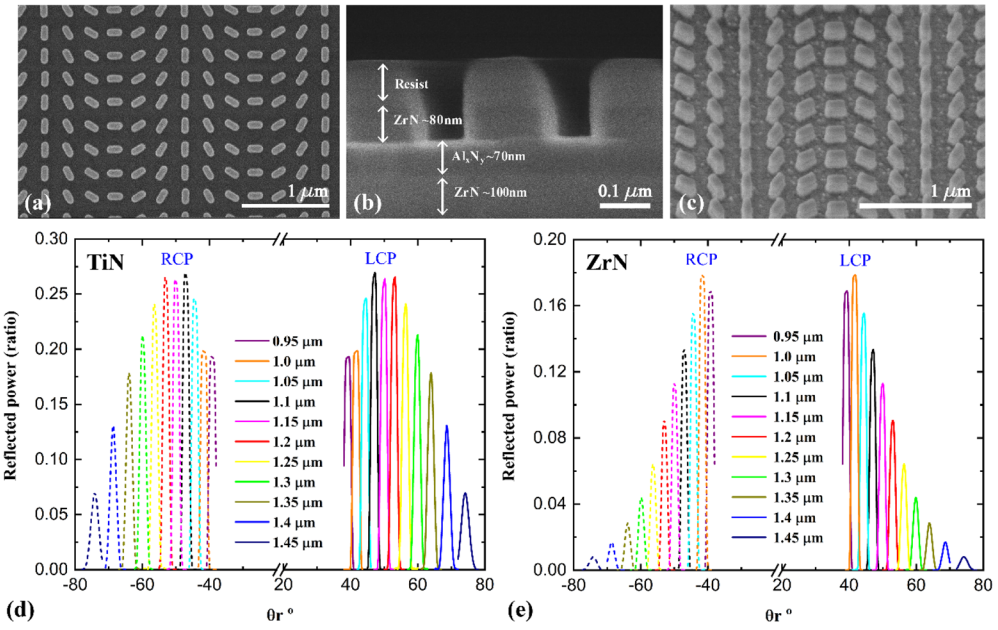

Figure 5. (a) Top-view, (b) cross-section, and (c) tilted (at 30°) scanning electron microscope (SEM) image of the fabricated metasurface. Images (a) and (b) are taken from a ZrN-based and (c) from a TiN-based fabricated sample with a 1.5 μm supercell period. Experimentally measured reflected power collected as a function of reflection angle, from the fabricated (d) TiN- and (e) ZrN-based metasurfaces for different frequency incident beams with left or right circular polarization.

efficiency of this first demonstration is slightly lower to a previous Au-based design[16] but offers a much broader bandwidth of operation (0.9−1.6 μm). Refractory TMNs have brought exciting opportunities to plasmonic devices with their high-temperature and mechanical stability, in addition to the metal-like optical properties and compatibility with CMOS processing. Although, their advantages are many and the materials are deemed promising for a long time, there have been very few demonstrations of real devices involving these transition metal nitrides. This first demonstration of phase gradient metasurfaces using the transition metal nitrides aims to fill this gap by successful integration of the new materials (and their stacks with other materials) in established device architectures. The processing techniques developed in this work can be translated to practical device demonstrations by utilizing low-cost, large-area nanostructuring techniques such as nanoimprint and conformal imprint lithography. We believe that this work will play a key role in shaping the future of transition metal nitrides based plasmonics, as well as in assimilating the material class into the arena of compact, durable, and cost-effective flat optics.

■ ASSOCIATED CONTENT

Supporting Information

The Supporting Information is available free of charge on the ACS Publications website at DOI: 10.1021/acsphotonics.8b00943.

Methods of thin film growth, metasurface fabrication, optical measurement, and numerical simulations; details on optical properties, VASE models, and discussion on the effect of material properties on the device performance (PDF)

■ AUTHOR INFORMATION

Corresponding Author

*E-mail: aeb@purdue.edu.

ORCID

Krishnakali Chaudhuri: 0000-0002-5988-7625

Notes

The authors declare no competing financial interest.

■ ACKNOWLEDGMENTS

The authors would like to acknowledge valuable discussions with colleague Jongbum Kim (Purdue University, University of Maryland) about fabrication methods during this work. We acknowledge partial funding support for this work by AFOSR MURI Grant FA9550-12-1-0389 and AFOSR Grant FA9550-17-1-0243.

■ REFERENCES

(1) Yu, N.; Capasso, F. Flat Optics with Designer Metasurfaces. *Nat. Mater.* **2014**, *13* (2), 139−150.
(2) Chen, H.-T.; Taylor, A. J.; Yu, N. A Review of Metasurfaces: Physics and Applications. *Rep. Prog. Phys.* **2016**, *79* (7), 076401.
(3) Chang, S.; Guo, X.; Ni, X. Optical Metasurfaces: Progress and Applications. *Annu. Rev. Mater. Res.* **2018**, *48* (1), 279−302.
(4) Arbabi, E.; Arbabi, A.; Kamali, S. M.; Horie, Y.; Faraji-Dana, M.; Faraon, A. MEMS-Tunable Dielectric Metasurface Lens. *Nat. Commun.* **2018**, *9* (1), 812.
(5) Khorasaninejad, M.; Chen, W. T.; Devlin, R. C.; Oh, J.; Zhu, A. Y.; Capasso, F. Metalenses at Visible Wavelengths: Diffraction-Limited Focusing and Subwavelength Resolution Imaging. *Science* **2016**, *352* (6290), 1190−1194.
(6) Chen, X.; Huang, L.; Mühlenbernd, H.; Li, G.; Bai, B.; Tan, Q.; Jin, G.; Qiu, C.-W.; Zhang, S.; Zentgraf, T. Dual-Polarity Plasmonic Metalens for Visible Light. *Nat. Commun.* **2012**, *3* (1), 1198.
(7) Huang, L.; Chen, X.; Mühlenbernd, H.; Zhang, H.; Chen, S.; Bai, B.; Tan, Q.; Jin, G.; Cheah, K.-W.; Qiu, C.-W.; Li, J.; Zentgraf, T.; Zhang, S. Three-Dimensional Optical Holography Using a Plasmonic Metasurface. *Nat. Commun.* **2013**, *4* (1), 2808.
(8) Zheng, G.; Mühlenbernd, H.; Kenney, M.; Li, G.; Zentgraf, T.; Zhang, S. Metasurface Holograms Reaching 80% Efficiency. *Nat. Nanotechnol.* **2015**, *10* (4), 308−312.

DOI: 10.1021/acsphotonics.8b00943
ACS Photonics 2019, 6, 99−106

(9) Wan, W.; Gao, J.; Yang, X. Full-Color Plasmonic Metasurface Holograms. *ACS Nano* **2016**, *10* (12), 10671−10680.
(10) Yu, N.; Aieta, F.; Genevet, P.; Kats, M. A.; Gaburro, Z.; Capasso, F. A Broadband, Background-Free Quarter-Wave Plate Based on Plasmonic Metasurfaces. *Nano Lett.* **2012**, *12* (12), 6328−6333.
(11) Pors, A.; Bozhevolnyi, S. I. Efficient and Broadband Quarter-Wave Plates by Gap-Plasmon Resonators. *Opt. Express* **2013**, *21* (3), 2942.
(12) Tahir, A. A.; Schulz, S. A.; De Leon, I.; Boyd, R. W. Design Principles for Wave Plate Metasurfaces Using Plasmonic L-Shaped Nanoantennas. *J. Opt.* **2017**, *19* (3), 035001.
(13) Liu, Z.; Li, Z.; Liu, Z.; Cheng, H.; Liu, W.; Tang, C.; Gu, C.; Li, J.; Chen, H.-T.; Chen, S.; Tian, J. Single-Layer Plasmonic Metasurface Half-Wave Plates with Wavelength-Independent Polarization Conversion Angle. *ACS Photonics* **2017**, *4* (8), 2061−2069.
(14) Zhu, A. Y.; Chen, W.-T.; Khorasaninejad, M.; Oh, J.; Zaidi, A.; Mishra, I.; Devlin, R. C.; Capasso, F. Ultra-Compact Visible Chiral Spectrometer with Meta-Lenses. *APL Photonics* **2017**, *2* (3), 036103.
(15) Colomban, P. The Use of Metal Nanoparticles to Produce Yellow, Red and Iridescent Colour, from Bronze Age to Present Times in Lustre Pottery and Glass: Solid State Chemistry, Spectroscopy and Nanostructure. *J. Nano Res.* **2009**, *8*, 109−132.
(16) Shaltout, A.; Liu, J.; Kildishev, A.; Shalaev, V. Photonic Spin Hall Effect in Gap−plasmon Metasurfaces for On-Chip Chiroptical Spectroscopy. *Optica* **2015**, *2* (10), 860.
(17) Maguid, E.; Yulevich, I.; Veksler, D.; Kleiner, V.; Brongersma, M. L.; Hasman, E. Photonic Spin-Controlled Multifunctional Shared-Aperture Antenna Array. *Science* **2016**, *352* (6290), 1202−1206.
(18) Shaltout, A.; Liu, J.; Shalaev, V. M.; Kildishev, A. V. Optically Active Metasurface with Non-Chiral Plasmonic Nanoantennas. *Nano Lett.* **2014**, *14* (8), 4426−4431.
(19) Zhao, Y.; Alù, A. Manipulating Light Polarization with Ultrathin Plasmonic Metasurfaces. *Phys. Rev. B: Condens. Matter Mater. Phys.* **2011**, *84*, 1−6.
(20) Bomzon, Z.; Kleiner, V.; Hasman, E. Pancharatnam−Berry Phase in Space-Variant Polarization-State Manipulations with Subwavelength Gratings. *Opt. Lett.* **2001**, *26* (18), 1424.
(21) Yang, Y.; Wang, W.; Moitra, P.; Kravchenko, I. I.; Briggs, D. P.; Valentine, J. Dielectric Meta-Reflectarray for Broadband Linear Polarization Conversion and Optical Vortex Generation. *Nano Lett.* **2014**, *14* (3), 1394−1399.
(22) Choudhury, S. M.; Wang, D.; Chaudhuri, K.; DeVault, C.; Kildishev, A. V.; Boltasseva, A.; Shalaev, V. M. Material Platforms for Optical Metasurfaces. *Nanophotonics* **2018**, *7* (6), 959−987.
(23) Wu, C.; Khanikaev, A. B.; Adato, R.; Arju, N.; Yanik, A. A.; Altug, H.; Shvets, G. Fano-Resonant Asymmetric Metamaterials for Ultrasensitive Spectroscopy and Identification of Molecular Monolayers. *Nat. Mater.* **2012**, *11* (1), 69−75.
(24) Jiang, L.; Zeng, S.; Ouyang, Q.; Dinh, X.-Q.; Coquet, P.; Qu, J.; He, S.; Yong, K.-T. Graphene-TMDC-Graphene Hybrid Plasmonic Metasurface for Enhanced Biosensing: A Theoretical Analysis. *Phys. Status Solidi A* **2017**, *214* (12), 1700563.
(25) Fan, J.-R.; Zhu, J.; Wu, W.-G.; Huang, Y. Plasmonic Metasurfaces Based on Nanopin-Cavity Resonator for Quantitative Colorimetric Ricin Sensing. *Small* **2017**, *13* (1), 1601710.
(26) Fang, J.; Wang, D.; DeVault, C. T.; Chung, T.-F.; Chen, Y. P.; Boltasseva, A.; Shalaev, V. M.; Kildishev, A. V. Enhanced Graphene Photodetector with Fractal Metasurface. *Nano Lett.* **2017**, *17* (1), 57−62.
(27) Costantini, D.; Lefebvre, A.; Coutrot, A.-L.; Moldovan-Doyen, I.; Hugonin, J.-P.; Boutami, S.; Marquier, F.; Benisty, H.; Greffet, J.-J. Plasmonic Metasurface for Directional and Frequency-Selective Thermal Emission. *Phys. Rev. Appl.* **2015**, *4* (1), 014023.
(28) Chaudhuri, K.; Alhabeb, M.; Wang, Z.; Shalaev, V. M.; Gogotsi, Y.; Boltasseva, A. Highly Broadband Absorber Using Plasmonic Titanium Carbide (MXene). *ACS Photonics* **2018**, *5* (3), 1115−1122.
(29) Argyropoulos, C.; Le, K. Q.; Mattiucci, N.; D'Aguanno, G.; Alù, A. Broadband Absorbers and Selective Emitters Based on Plasmonic Brewster Metasurfaces. *Phys. Rev. B: Condens. Matter Mater. Phys.* **2013**, *87* (20), 205112.
(30) Cui, T.-J.; Liu, S.; Li, L.-L. Information Entropy of Coding Metasurface. *Light: Sci. Appl.* **2016**, *5* (11), No. e16172-e16172.
(31) Kamali, S. M.; Arbabi, E.; Arbabi, A.; Horie, Y.; Faraji-Dana, M.; Faraon, A. Angle-Multiplexed Metasurfaces: Encoding Independent Wavefronts in a Single Metasurface under Different Illumination Angles. *Phys. Rev. X* **2017**, *7* (4), 41056.
(32) Walter, F.; Li, G.; Meier, C.; Zhang, S.; Zentgraf, T. Ultrathin Nonlinear Metasurface for Optical Image Encoding. *Nano Lett.* **2017**, *17* (5), 3171−3175.
(33) West, P.; Ishii, S.; Naik, G. V.; Emani, N.; Boltasseva, A. *Identifying Low-Loss Plasmonic Materials.* SPIE, **2010**, DOI: 10.1117/2.1201009.003167.
(34) Khurgin, J. B. How to Deal with the Loss in Plasmonics and Metamaterials. *Nat. Nanotechnol.* **2015**, *10* (1), 2−6.
(35) Jahani, S.; Jacob, Z. All-Dielectric Metamaterials. *Nat. Nanotechnol.* **2016**, *11* (1), 23−36.
(36) Decker, M.; Staude, I.; Falkner, M.; Dominguez, J.; Neshev, D. N.; Brener, I.; Pertsch, T.; Kivshar, Y. S. High-Efficiency Dielectric Huygens' Surfaces. *Adv. Opt. Mater.* **2015**, *3* (6), 813−820.
(37) Nielsen, M. G.; Bozhevolnyi, S. I. *Gap Plasmon-Based Metasurfaces: Fundamentals and Applications*; Engheta, N., Noginov, M. A., Zheludev, N. I., Eds.; 2014; Vol. *9160*, p 916006.
(38) Sun, S.; Yang, K.; Wang, C.; Juan, T.; Chen, W. T.; Liao, C. Y.; He, Q.; Xiao, S.; Kung, W.; Guo, G.; Zhou, L.; Tsai, D. P. High-Efficiency Broadband Anomalous Reflection by Gradient Meta-Surfaces. *Nano Lett.* **2012**, *12* (12), 6223−6229.
(39) Bozhevolnyi, S. I.; Søndergaard, T. General Properties of Slow-Plasmon Resonant Nanostructures: Nano-Antennas and Resonators. *Opt. Express* **2007**, *15* (17), 10869−10877.
(40) Pors, A.; Albrektsen, O.; Radko, I. P.; Bozhevolnyi, S. I. Gap Plasmon-Based Metasurfaces for Total Control of Reflected Light. *Sci. Rep.* **2013**, *3*, 2155.
(41) Naik, G. V.; Shalaev, V. M.; Boltasseva, A. Alternative Plasmonic Materials: Beyond Gold and Silver. *Adv. Mater.* **2013**, *25* (24), 3264−3294.
(42) West, P. R.; Ishii, S.; Naik, G. V.; Emani, N. K.; Shalaev, V. M.; Boltasseva, A. Searching for Better Plasmonic Materials. *Laser Photon. Rev.* **2010**, *4* (6), 795−808.
(43) Doering, R.; Nishi, Y. *Handbook of Semiconductor Manufacturing Technology*, 2nd ed.; CRC Press, 2007.
(44) Franey, J. P.; Kammlott, G. W.; Graedel, T. E. The Corrosion of Silver by Atmospheric Sulfurous Gases. *Corros. Sci.* **1985**, *25* (2), 133−143.
(45) Guler, U.; Boltasseva, A.; Shalaev, V. M. Refractory Plasmonics. *Science* **2014**, *344* (6181), 263−264.
(46) Shah, D.; Reddy, H.; Kinsey, N.; Shalaev, V. M.; Boltasseva, A. Optical Properties of Plasmonic Ultrathin TiN Films. *Adv. Opt. Mater.* **2017**, *5* (13), 1700065.
(47) Kinsey, N.; Ferrera, M.; Naik, G. V.; Babicheva, V. E.; Shalaev, V. M.; Boltasseva, A. Experimental Demonstration of Titanium Nitride Plasmonic Interconnects. *Opt. Express* **2014**, *22* (10), 12238.
(48) Patsalas, P.; Kalfagiannis, N.; Kassavetis, S.; Abadias, G.; Bellas, D. V.; Lekka, C.; Lidorikis, E. Conductive Nitrides: Growth Principles, Optical and Electronic Properties, and Their Perspectives in Photonics and Plasmonics. *Mater. Sci. Eng., R* **2018**, *123*, 1−55.
(49) Patsalas, P.; Logothetidis, S. Interface Properties and Structural Evolution of TiN/Si and TiN/GaN Heterostructures. *J. Appl. Phys.* **2003**, *93* (2), 989−998.
(50) Liu, Y.; Matsukawa, T.; Endo, K.; Masahara, M.; Ishii, K.; O'uchi, S. i.; Yamauchi, H.; Tsukada, J.; Ishikawa, Y.; Suzuki, E. Advanced FinFET CMOS Technology: TiN-Gate, Fin-Height Control and Asymmetric Gate Insulator Thickness 4T-FinFETs. In *2006 International Electron Devices Meeting*; 2006; pp 1−4.
(51) Garcia, A. S.; Diniz, J. A.; Swart, J. W.; Lima, L. P. B.; dos Santos, M. V. P. Formation and Characterization of Tin Layers for Metal Gate Electrodes of CMOS Capacitors. In *2014 International*

DOI: 10.1021/acsphotonics.8b00943
ACS Photonics 2019, 6, 99−106

Caribbean Conference on Devices, Circuits and Systems (ICCDCS); 2014; pp 1−6.
(52) Reinholdt, A.; Pecenka, R.; Pinchuk, A.; Runte, S.; Stepanov, A. L.; Weirich, T. E.; Kreibig, U. Structural, Compositional, Optical and Colorimetric Characterization of TiN-Nanoparticles. *Eur. Phys. J. D* **2004**, *31* (1), 69−76.
(53) Naik, G. V.; Kim, J.; Boltasseva, A. Oxides and Nitrides as Alternative Plasmonic Materials in the Optical Range. *Opt. Mater. Express* **2011**, *1* (6), 1090−1099.
(54) Briggs, J. A.; Naik, G. V.; Petach, T. A.; Baum, B. K.; Goldhaber-Gordon, D.; Dionne, J. A. Fully CMOS-Compatible Titanium Nitride Nanoantennas. *Appl. Phys. Lett.* **2016**, *108* (5), 051110.
(55) Yu, I.-S.; Cheng, H.-E.; Chang, C.-C.; Lin, Y.-W.; Chen, H.-T.; Wang, Y.-C.; Yang, Z.-P. Substrate-Insensitive Atomic Layer Deposition of Plasmonic Titanium Nitride Films. *Opt. Mater. Express* **2017**, *7* (3), 777.
(56) Wang, Y.; Capretti, A.; Dal Negro, L. Wide Tuning of the Optical and Structural Properties of Alternative Plasmonic Materials. *Opt. Mater. Express* **2015**, *5* (11), 2415.
(57) Sugavaneshwar, R. P.; Ishii, S.; Dao, T. D.; Ohi, A.; Nabatame, T.; Nagao, T. Fabrication of Highly Metallic TiN Films by Pulsed Laser Deposition Method for Plasmonic Applications. *ACS Photonics* **2018**, *5* (3), 814−819.
(58) Lalisse, A.; Tessier, G.; Plain, J.; Baffou, G. Plasmonic Efficiencies of Nanoparticles Made of Metal Nitrides (TiN, ZrN) Compared with Gold. *Sci. Rep.* **2016**, *6* (1), 38647.
(59) Kinsey, N.; Syed, A. A.; Courtwright, D.; DeVault, C.; Bonner, C. E.; Gavrilenko, V. I.; Shalaev, V. M.; Hagan, D. J.; Van Stryland, E. W.; Boltasseva, A. Effective Third-Order Nonlinearities in Metallic Refractory Titanium Nitride Thin Films. *Opt. Mater. Express* **2015**, *5* (11), 2395.
(60) Capretti, A.; Wang, Y.; Engheta, N.; Dal Negro, L. Comparative Study of Second-Harmonic Generation from Epsilon-Near-Zero Indium Tin Oxide and Titanium Nitride Nanolayers Excited in the Near-Infrared Spectral Range. *ACS Photonics* **2015**, *2* (11), 1584−1591.
(61) Gui, L.; Bagheri, S.; Strohfeldt, N.; Hentschel, M.; Zgrabik, C. M.; Metzger, B.; Linnenbank, H.; Hu, E. L.; Giessen, H. Nonlinear Refractory Plasmonics with Titanium Nitride Nanoantennas. *Nano Lett.* **2016**, *16* (9), 5708−5713.
(62) Reddy, H.; Guler, U.; Kudyshev, Z.; Kildishev, A. V.; Shalaev, V. M.; Boltasseva, A. Temperature-Dependent Optical Properties of Plasmonic Titanium Nitride Thin Films. *ACS Photonics* **2017**, *4* (6), 1413−1420.
(63) Bouillard, J.-S. G.; Dickson, W.; O'Connor, D. P.; Wurtz, G. A.; Zayats, A. V. Low-Temperature Plasmonics of Metallic Nanostructures. *Nano Lett.* **2012**, *12* (3), 1561−1565.
(64) Ishii, S.; Sugavaneshwar, R. P.; Nagao, T. Titanium Nitride Nanoparticles as Plasmonic Solar Heat Transducers. *J. Phys. Chem. C* **2016**, *120* (4), 2343−2348.
(65) Chirumamilla, M.; Chirumamilla, A.; Yang, Y.; Roberts, A. S.; Kristensen, P. K.; Chaudhuri, K.; Boltasseva, A.; Sutherland, D. S.; Bozhevolnyi, S. I.; Pedersen, K. Large-Area Ultrabroadband Absorber for Solar Thermophotovoltaics Based on 3D Titanium Nitride Nanopillars. *Adv. Opt. Mater.* **2017**, *5*, 1700552.
(66) Naik, G. V.; Schroeder, J. L.; Ni, X.; Kildishev, A. V.; Sands, T. D.; Boltasseva, A. Titanium Nitride as a Plasmonic Material for Visible and Near-Infrared Wavelengths. *Opt. Mater. Express* **2012**, *2* (4), 478.
(67) Zgrabik, C. M.; Hu, E. L. Optimization of Sputtered Titanium Nitride as a Tunable Metal for Plasmonic Applications. *Opt. Mater. Express* **2015**, *5* (12), 2786.
(68) Li, W.; Guler, U.; Kinsey, N.; Naik, G. V.; Boltasseva, A.; Guan, J.; Shalaev, V. M.; Kildishev, A. V. Refractory Plasmonics with Titanium Nitride: Broadband Metamaterial Absorber. *Adv. Mater.* **2014**, *26* (47), 7959−7965.
(69) Guler, U.; Ndukaife, J. C.; Naik, G. V.; Nnanna, A. G. A.; Kildishev, A. V.; Shalaev, V. M.; Boltasseva, A. Local Heating with Lithographically Fabricated Plasmonic Titanium Nitride Nanoparticles. *Nano Lett.* **2013**, *13* (12), 6078−6083.
(70) Hu, J.; Ren, X.; Reed, A. N.; Reese, T.; Rhee, D.; Howe, B.; Lauhon, L. J.; Urbas, A. M.; Odom, T. W. Evolutionary Design and Prototyping of Single Crystalline Titanium Nitride Lattice Optics. *ACS Photonics* **2017**, *4* (3), 606−612.
(71) Lee, W.; A, W. B. Protein Secondary Structure Analyses from Circular Dichroism Spectroscopy: Methods and Reference Databases. *Biopolymers* **2007**, *89* (5), 392−400.
(72) Freedman, T. B.; Cao, X.; Dukor, R. K.; Nafie, L. A. Absolute Configuration Determination of Chiral Molecules in the Solution State Using Vibrational Circular Dichroism. *Chirality* **2003**, *15*, 743−758.
(73) Tsankov, D.; Eggimann, T.; Wieser, H. Alternative Design for Improved FT-IR/VCD Capabilities. *Appl. Spectrosc.* **1995**, *49* (1), 132−138.
(74) Liu, Y.; Ke, Y.; Wen, S.; Luo, H. Photonic Spin Hall Effect in Metasurfaces: A Brief Review. *Nanophotonics* **2017**, *6* (1), 51−70.
(75) Shitrit, N.; Yulevich, I.; Maguid, E.; Ozeri, D.; Veksler, D.; Kleiner, V.; Hasman, E. Spin-Optical Metamaterial Route to Spin-Controlled Photonics. *Science* **2013**, *340* (6133), 724−726.
(76) Jung, J.; Søndergaard, T.; Bozhevolnyi, S. I. Gap Plasmon-Polariton Nanoresonators: Scattering Enhancement and Launching of Surface Plasmon Polaritons. *Phys. Rev. B: Condens. Matter Mater. Phys.* **2009**, *79* (3), 035401.
(77) Jones, R. C. A New Calculus for the Treatment of Optical Systems. IV. *J. Opt. Soc. Am.* **1942**, *32* (1), 486−494.
(78) Bomzon, Z.; Biener, G.; Kleiner, V.; Hasman, E. Space-Variant Pancharatnam−Berry Phase Optical Elements with Computer-Generated Subwavelength Gratings. *Opt. Lett.* **2002**, *27* (13), 1141.
(79) Berry, M. V. The Adiabatic Phase and Pancharatnam's Phase for Polarized Light. *J. Mod. Opt.* **1987**, *34* (11), 1401−1407.
(80) Yu, N.; Genevet, P.; Kats, M. A.; Aieta, F.; Tetienne, J.-P.; Capasso, F.; Gaburro, Z. Light Propagation with Phase Discontinuities: Generalized Laws of Reflection and Refraction. *Science* **2011**, *334* (6054), 333−337.
(81) Shen, P.-T.; Sivan, Y.; Lin, C.-W.; Liu, H.-L.; Chang, C.-W.; Chu, S.-W. Temperature- and Roughness- Dependent Permittivity of Annealed/Unannealed Gold Films. *Opt. Express* **2016**, *24* (17), 19254.

DOI: 10.1021/acsphotonics.8b00943
ACS Photonics 2019, 6, 99−106